Hindawi
International Journal of Energy Research
Volume 2024, Article ID 3167699, 13 pages
https://doi.org/10.1155/2024/3167699

Research Article

Excellent Bifunctional Water Electrolysis Activities of α-MoO_3/AC Nanocomposites

Sankar Sekar,[1,2] **Ji-Seop Yun**,[1] **Seoyeon Park**,[1] **Deuk Young Kim**,[1,2] **Youngmin Lee**,[1,2] **and Sejoon Lee**[1,2]

[1]*Department of Semiconductor Science, Dongguk University-Seoul, Seoul 04620, Republic of Korea*
[2]*Quantum-Functional Semiconductor Research Center, Dongguk University-Seoul, Seoul 04620, Republic of Korea*

Correspondence should be addressed to Sejoon Lee; sejoon@dongguk.edu

Received 13 March 2023; Revised 11 January 2024; Accepted 18 January 2024; Published 25 January 2024

Academic Editor: Mohamed Zbair

Electrocatalytic water splitting is a cost-effective and environment-friendly technique for producing oxygen and hydrogen through the oxygen/hydrogen evolution reaction (OER/HER). Developing the highly active and stable electrocatalyst, particularly for bifunctional water electrolysis (*i.e.*, both OER and HER), is still a formidable challenge. Herein, we demonstrated the enhanced bifunctional water splitting activities by utilizing the molybdenum trioxide-anchored activated carbon (MoO_3/AC) nanocomposites. The MoO_3/AC samples were fabricated by the ultrasonication method using sol-gel synthesized MoO_3 and biomass-derived AC, and they displayed a nanostreusel-like morphology with spherical MoO_3 nanoparticle-decorated AC nanosheets. For the water electrolysis test, the MoO_3/AC nanocomposites exhibited the excellent bifunctional electrocatalytic OER and HER performances with low overpotential and small Tafel slope values. Through analyzing the material characteristics and the electrochemical properties of MoO_3/AC, it was found that the superb bifunctional OER-HER activities were attributed to the synergistic effects from the hybridization of highly conductive AC and electrochemically active α-MoO_3. The results pronounce that the MoO_3/AC nanocomposites possess an aptitude as a superb bifunctional OER/HER electrocatalyst for high-performance water electrolysis.

1. Introduction

Due to its zero-carbon emission as well as high energy density, hydrogen has emerged as a promising green energy source that can alternate the fossil fuels and release the environmental crisis [1–3]. Electrocatalytic water splitting is a fascinating technique for producing the renewable hydrogen energy source from water because the method possesses many advantages such as ecofriendliness, recyclability, and sustainability [4–8]. Water electrolysis consists of two basic half-cell reactions at the anode and the cathode; *i.e.*, the oxygen evolution reaction (OER) takes place at the anode, and in turn, the hydrogen evolution reaction (HER) occurs at the cathode [9–11]. For OER and HER, Ir/Ru- and Pt-based materials were typically used as electrode materials because of their superior electrocatalytic performances [12–15]. However, the low natural abundance and the high cost of both novel metal and rare earth material would somewhat restrict their practical applications [16–19]. Meanwhile, it is well known that OER is less effective than HER because of its sluggish reaction kinetics and high energy consumption [20–23]. To perform the high electrocatalytic water splitting activities of both OER and HER, therefore, developing a highly efficient bifunctional electrocatalyst is vital. In practical application point of view, particularly, finding a highly durable and low-cost electrode material is of great essence.

Recently, transition metal oxides (TMOs) have garnered ample attention as a proficient catalyst because of their high electrochemical activity and cost-effectiveness [24–28]. Among various TMOs, molybdenum trioxide (MoO_3) has emerged as an efficient electrocatalyst because of its double-layer planar structure, nontoxicity, high stability, and intrinsic characteristics [29–33]. Crystallographically, MoO_3 possesses three different types of crystalline phases (*i.e.*, α, β, and h) [34–36]. Among them, orthorhombic α-

MoO_3 consists of the octahedral MoO_6 double-layer structure that performs high electrochemical reactivity and good thermodynamic stability [37, 38]. These play a key role for promoting the oxygen-associated reaction during the electrocatalytic water splitting process [33, 36]. Accordingly, many research groups have attempted to fabricate high-quality α-MoO_3 by utilizing several experimental methods (*e.g.*, microwave-assisted chemical synthesis [39], ultrasonication [40], water-based exfoliation [41], hydrothermal growth [38, 42], wet chemical process [43, 44], sol-gel [45–47], and ball milling [48]). Despite such substantial efforts, the electrocatalytic performances of α-MoO_3 are still unsatisfiable because of its small electrochemically active site, poor ionic conductivity, poor electronic conductivity, and sluggish kinetics [33, 49]. Aiming at improving the electrocatalytic activity of α-MoO_3, therefore, it was intensively tried to materialize the α-MoO_3-based nanocomposites by hybridizing with various carbonaceous nanostructures (*e.g.*, carbon nanotube [50], graphene [51], graphene oxide [52], and activated carbon (AC) [53]). Among those, AC is of good use for fabricating the MoO_3/AC nanocomposites as a high-performance OER and HER catalyst [53]. This is because high conductivity and large surface area of AC could help enhance the electronic charge transfer and the ionic motion, respectively. Generally, AC could be synthesized by two different approaches, *i.e.*, physical (thermal) and chemical activation processes. In physical activation, initially, the raw material was carbonized and subsequently gasified at higher temperatures (500–1000°C) in a stream of oxidizing gas (*e.g.*, air, steam, and CO_2) [54, 55]. For chemical activation, the precursor material is mixed with the chemical agents (*e.g.*, KOH, $ZnCl_2$, NaOH, H_2SO_4, LiOH, and H_3PO_4) and followed by annealing at moderate temperatures (400–700°C) [56–58]. In both cases, the textural characteristics and the pore size distribution of AC can also be modulated by changing the precursors, ambient gases, and activation agents [59]. When using biomass-derived AC, furthermore, there are additional advantages such as a cost-effectiveness, an ecofriendliness, a massive abundance, and a fast regeneration [60–63]. For instance, Hoang et al. [64] prepared the hybrid Ni/NiO nanocomposite with N-doped biomass AC and exhibited an overpotential of 346 mV (for OER) and 180 mV (for HER) in 0.1 M KOH. Sangeetha et al. [53] prepared the biomass AC-decorated *h*-MoO_3 nanocomposite *via* the hydrothermal method and showed an overpotential of 282 mV and Tafel slope of 169 mV/dec for HER in 0.5 sulphuric acid. Kou et al. [65] synthesized the NiO-based nanocomposites decorated with nitrogen-doped biomass AC dots and demonstrated an overpotential of 380 mV at 10 mA/cm^2 for OER. Yaseen et al. [66] fabricated the hierarchical Co/MoO_2@N-doped biomass AC nanocomposites *via* the simple annealing process and exhibited the excellent OER and HER activity with a low overpotential of 272 mV and 130 mV in 1 M KOH. In spite of all the above benefits from both MoO_3 and biomass AC, the electrocatalytic activity of the MoO_3/AC nanocomposites has rarely been investigated [53].

All these prompt us to study on the fabrication of robust MoO_3/AC that could act as an excellent bifunctional OER/HER electrocatalyst. In this study, we synthesized and characterized the MoO_3/AC nanocomposites that were devised through facile ultrasonication by utilizing the sol-gel synthesized MoO_3 nanoparticles and the biomass human hair-derived AC nanosheets. From the fabricated MoO_3/AC nanocomposites, we found that the excellent bifunctional electrocatalytic water splitting activities could be achievable. For example, low overpotential values (OER: 280 mV at 10 mA/cm^2 and HER: 353 mV at 10 mA/cm^2) were recorded from MoO_3/AC. Herein, the material characteristics and the electrocatalytic performances are thoroughly assessed and discussed in detail.

2. Experimental Details

2.1. Growth of MoO_3 Nanoparticles. Figure 1 represents a schematic diagram of the fabrication procedure for obtaining high-quality MoO_3/AC. Firstly, the α-MoO_3 nanoparticles were synthesized through the sol-gel process by using ammonium heptamolybdate ($(NH_4)_6Mo_7O_{24}$) and nitric acid (HNO_3). As a primary task, $(NH_4)_6Mo_7O_{24}$ (6 g) was added into deionized (DI) water (30 mL). After continuous stirring for 10 min, HNO_3 (15 mL) was injected drop-by-drop into the above aqueous ammonium heptamolybdate solution and subsequently stirred for 4 h at 100°C in a sand bath. After cooling down to 27°C, the mixture solution was filtered and washed five times in DI water and ethanol. Then, the suspension was dried for 10 h at 80°C. Finally, the α-MoO_3 nanoparticles were obtained by performing postgrowth thermal annealing at 700°C for 3 h. Here, we note that no additional purification was performed for all the used materials that were purchased from Sigma-Aldrich (St. Louis, MO, USA).

2.2. Derivation of AC Nanosheets. The AC nanosheets were derived from the biomass resource of human hair (HH) through thermal carbonization and KOH activation. Initially, the collected biomass HH bundles were cleaned and rinsed with DI water (three times for each) and dried in air for 24 h. After that, the carbonization of HH was carried out in air at 300°C for 60 min. Then, the mixture of carbonized HH ashes (5 g) and KOH (20 g) was prepared by utilizing a mortar. After subsequent annealing at 600°C for 120 min in a muffle furnace, the KOH-activated HH ashes were rinsed for 12 h in DI water to extract potassium and its related precipitates. Finally, the pure HH-derived AC nanosheets were collected *via* filtrating, rinsing, and drying (120°C, 12 h). The experimental procedures in more detail for obtaining high-quality HH-derived AC were reported elsewhere in our previous study [18].

2.3. Fabrication of MoO_3/AC Nanocomposites. The nanocomposites of MoO_3/AC were fabricated by the facile ultrasonication method. Initially, the MoO_3 nanoparticles (1 g) were blended and stirred in DI water (100 mL) for 15 min. Next, the AC nanosheets (0.5 g) were added into the above MoO_3-blended aqueous solution and stirred for 30 min. Subsequently, the MoO_3-AC mixture solution was sonicated for 1 h (f_{ultra} = 35 kHz, P_{ultra} = 240 W). During the ultrasonication step, the high-power ultrasound supplies an excessive energy enough to cleave and break the big clusters into the

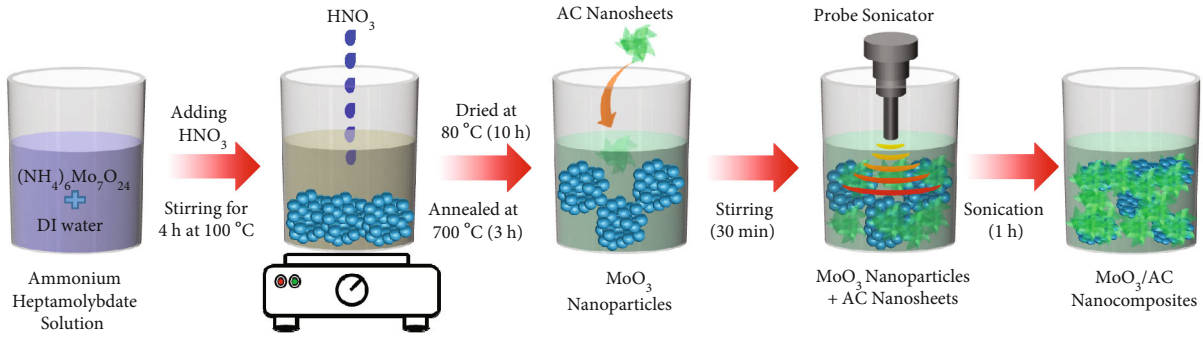

FIGURE 1: Experimental procedures for the fabrication of the MoO_3 nanoparticles and the MoO_3/AC nanocomposites.

tiny species [67–69]. Then, the dispersity of the nanoparticles could be increased in the entire composite system. After sonication, the powder-type MoO_3/AC nanocomposites were obtained *via* sieving, cleaning, rinsing, and drying (120°C, 8 h) of the prepared colloidal suspension.

2.4. Material Characterization. The structural and the vibrational properties of the prepared materials (*i.e.*, MoO_3, AC, and MoO_3/AC) were examined by X-ray diffractometry (XRD) using an Ultima IV system (Rigaku, Tokyo, Japan) and Raman scattering spectroscopy using a LabRAM HR-800 system (Jobin Yvon, Longjumeau, France), respectively. In addition, the morphological structure and the chemical composition of MoO_3 and MoO_3/AC were monitored by field emission scanning electron microscopy (FE-SEM) and *in situ* energy-dispersive X-ray spectroscopy (EDX), respectively, using an Inspect F50 system (FEI, Mahwah, NJ, USA). Furthermore, the microstructural properties of the samples were characterized by transmission electron microscopy (TEM) using a JEM 2100F system (JEOL, Tokyo, Japan).

2.5. Electrocatalytic Measurements. The water electrolysis characteristics of MoO_3 and MoO_3/AC were assessed by using a VersaSTAT 3 workstation (Ametek Scientific Instruments, Berwyn, PA, USA). To examine the electrocatalytic OER and HER performances, as a primary task, the conventional three-electrode system was prepared in a KOH solution (1 M). Firstly, the working electrodes were devised by using the bare MoO_3 nanoparticles and the MoO_3/AC nanocomposites. For this step, initially, each catalyst (*i.e.*, either MoO_3 or MoO_3/AC) was blended with N-methyl-2-pyrrolidinone and coated onto the stainless steel substrate (1 cm × 1 cm). Thereafter, the prepared substrates were dried for 8 h at 180°C to cure the active materials. To configure the three-electrode system, the counter electrode of platinum mesh (Nilaco Co., Tokyo, Japan) and the reference electrode of saturated calomel (Sanxin, Shenyang, China) were also prepared. Then, the cyclic voltammetry (CV) measurements were conducted at the potential window of 0.0–0.5 V under various scan rates of 10–100 mV/s. Additionally, the linear sweep voltammetry (LSV) characteristics were measured at potential windows of -0.1–1 V (for OER) and -1.8–0 V (for HER) under the scan rate of 1.0 mV/s. Furthermore, the chronopotentiometric (CP) characteristics of the prepared materials were investigated upon varying the applied current density (*i.e.*, "10 → 20 → 30 → 40 → 50 → 100 mA/cm^2 for OER" and "-10 → -20 → -30 → -40 → -50 → -100 mA/cm^2 for HER"). Here, the working electrodes were polarized at every current densities, and each polarization state at each current density was maintained for 10 min. To examine the electrical properties of MoO_3 and MoO_3/AC, furthermore, the electrochemical impedance spectroscopy (EIS) characteristics were also evaluated at 1 Hz–10 kHz.

3. Results and Discussion

Figure 2(a) shows the crystallographic properties of MoO_3 and MoO_3/AC. In both samples, the polycrystalline XRD patterns were detected at 12.78, 23.42, 25.74, 27.33, 33.71, 35.50, 39.02, 45.67, 46.34, 49.26, 58.83, 64.47, and 67.53°, which were sprouted from the lattice planes of (020), (110), (040), (021), (111), (041), (060), (200), (210), (002), (081), (062), and (0100) of orthorhombic α-MoO_3 (JCPDS card no.: 05-0508 [70–73]), respectively. No secondary phases in both MoO_3 and MoO_3/AC indicate the high crystal quality of the synthesized samples. Here, we notice that the absence of carbon-related peaks in MoO_3/AC is thought as resulting from the small volume of the AC nanosheets in the entire MoO_3/AC composites. The average crystallite distribution sizes were calculated to be 45 and 32 nm for MoO_3 and MoO_3/AC, respectively, by using Scherrer's formula, as follows [74, 75]:

$$D = \frac{K\lambda}{\beta \cos\theta}, \quad (1)$$

where K, θ, λ, and β are the Scherrer constant, Bragg angle, X-ray wavelength, and full width at half-maximum in radian, respectively. Such a result is thought as attributing to the sonochemical exfoliation of the MoO_3 particles (*i.e.*, interconnected $n$$MoO_3$ → exfoliated $MoO_{3(n)}$), as discussed later.

The vibrational properties of MoO_3 and MoO_3/AC were further characterized by the Raman scattering spectroscopy. As can be seen from Figure 2(b), both MoO_3 and MoO_3/AC exhibited the Raman peaks at 122, 150, 190, 214, 239, 282, 334, 374, 466, 661, 814, and 992 cm^{-1}, arising from the local vibrations in orthorhombic α-MoO_3 [76]. The Raman scattering mode at 992 cm^{-1} originates from the stretching vibration of terminal oxygen (Mo^{6+}=O), which is indicative of the layered α-MoO_3 structure [77]. The strong Raman peak at 814 cm^{-1} comes from the stretching vibration of

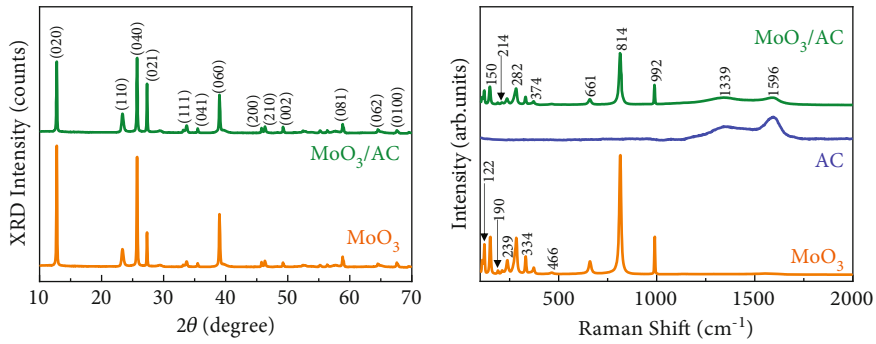

Figure 2: (a) XRD patterns of the MoO_3 nanoparticles and the MoO_3/AC nanocomposites. (b) Raman spectra of the MoO_3 nanoparticles, AC nanosheets, and the MoO_3/AC nanocomposites.

bicoordinated oxygen (Mo-O-Mo), which is corner-shared in two MoO_6 octahedra [78]. The peak at 661 cm^{-1} corresponds to the stretching vibration mode of triply coordinated oxygen (Mo_3-O), where the edge-shared oxygen atom mutually exists with three octahedra [79]. Asymmetric O-Mo-O bending and stretching are observed at 466 cm^{-1}. The Raman scattering modes at 374 and 334 cm^{-1} are associated with the O-Mo-O scissoring and bending vibrations, respectively [80]. The vibrational modes at 282, 239, 214,190, 150, and 122 cm^{-1} are credited to the wagging and twisting modes of O=Mo=O as well as MoO_4R_c rotational rigid chains [76, 81]. In the case of MoO_3/AC, one can see that there are two additional Raman scattering features at 1339 and 1596 cm^{-1}. Through double-checking with the bare AC nanosheets (Figure 2(b)), the former and the latter were confirmed to originate from the D and G bands of graphitized 2D AC, respectively [48, 63]. The D band arises from the disordered graphitic AC, and the G band belongs to the E_{2g} vibrational Raman scattering mode at sp^2-hybridized carbon lattices [82, 83]. The large intensity ratio of I_G/I_D (≈1.02) implies that the AC nanosheets in MoO_3/AC were highly graphitized with small numbers of stacked layers [84–92]. Thus, one can conjecture the present MoO_3/AC nanocomposites to comprise highly conductive AC that may improve the electrical conductivity of the entire MoO_3/AC nanocomposite system.

Figure 3 displays the morphological properties of the synthesized materials. In the case of MoO_3, the sample exhibited the nanoparticle-interconnected cluster-like morphology (Figures 3(a) and 3(b)). After sonicating the MoO_3 nanoparticles with the biomass HH-derived AC nanosheets (see also Figure S1 for the AC morphology), the sample exhibited the MoO_3/AC nanocomposite structure where the MoO_3 nanoparticles were aggregated with the cleaved AC nanosheets (Figures 3(c) and 3(d)). Here, it should be noticed that the MoO_3 particle size was much decreased after ultrasonication (see also Figure 4). Namely, the average particle size was reduced from 600 nm (bare MoO_3) to 200 nm (MoO_3/AC composite). This can be explained by the following ultrasonication mechanism. During ultrasonication in the aqueous solution, H_2O renders the two important radicals that can promote the sonochemical reaction; *i.e.*, one is hydrogen (H^*) and the other is hydroxyl (OH^*). These two radicals play key roles as the reductants during the sonication process [93–97]. Namely, when applying high ultrasonic power in H_2O, the bigger MoO_3 particles (*i.e.*, interconnected $nMoO_3$) would be cleaved and collapsed so that the smaller MoO_3 particles (*i.e.*, exfoliated $MoO_{3(n)}$) could be formed *via* the following reactions:

$$H_2O \underset{\text{Sonication}}{\longrightarrow} OH^* + H^* \quad (2)$$

$$nMoO_3 + OH^* + H^* \underset{\text{Sonication}}{\longrightarrow} MoO_{3\,(n)} \quad (3)$$

$$nMoO_3 + AC + OH^* + H^* \underset{\text{Sonication}}{\longrightarrow} MoO_{3\,(n)} - AC - MoO_{3\,(n)} \quad (4)$$

From the *in situ* EDX measurements (Figures 3(e) and 3(f)), it was confirmed that both MoO_3 and MoO_3/AC were composed of their own elements of Mo, O, and C. Here, it should be noted that the Pt peaks in the EDX spectra were arisen from the ultrathin Pt layer, which was coated onto the sample surface before the FE-SEM measurements to minimize the electron charging effect.

To monitor the microstructural insights into both MoO_3 and MoO_3/AC, TEM measurements were carried out. The MoO_3 sample exhibited a typical topography of the colloidal nanoparticles where the spherical MoO_3 nanoparticles were interconnected with each other (Figures 4(a) and 4(b)). As depicted in Figure 4(c), one can confirm the interplanar spacing of MoO_3 to be 0.38 nm (*i.e.*, direction of d_{100}), which coincides with that of orthorhombic (110) α-MoO_3 [98, 99]. Furthermore, the SAED pattern clearly showed the circularly dispersed spots, presenting a polycrystalline nature of orthorhombic α-MoO_3 [78, 100] (Figure 4(d)). Different from bare MoO_3, the MoO_3/AC nanocomposites clearly exhibited an intertwingled texture of the AC nanosheet-encapsulated spherical MoO_3 nanoparticles (Figures 4(e) and 4(f)). Moreover, it can be seen from the high-resolution TEM image that the crystallized spherical MoO_3 nanoparticles were aggregated with the amorphous AC nanosheets (Figure 4(g)). The coexistence of both ring patterns (*i.e.*, amorphous AC [56, 101]) and circularly dispersed spots (*i.e.*, polycrystalline MoO_3 [78, 100]) further verifies the effective formation of the MoO_3/AC composites (Figure 4(h)).

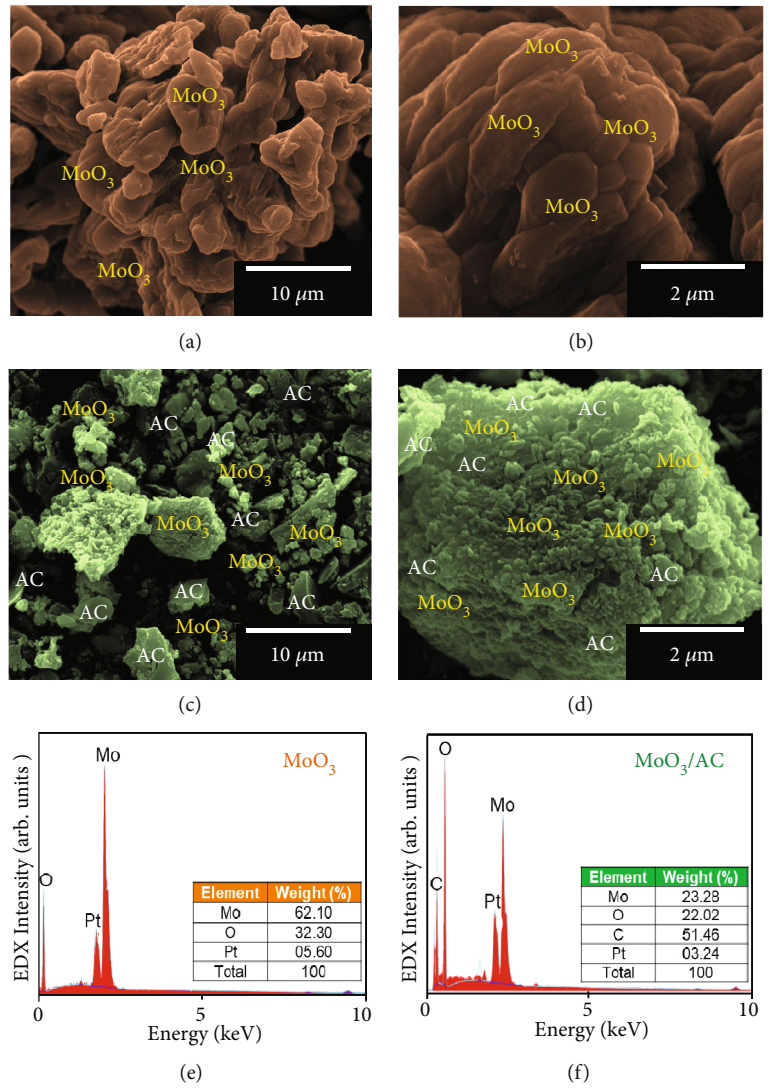

FIGURE 3: (a) Low- and (b) high-magnification FE-SEM images of the MoO_3 nanoparticles and (c) low- and (d) high-magnification FE-SEM images of the MoO_3/AC nanocomposites. EDX spectra of the (e) MoO_3 nanoparticles and the (f) MoO_3/AC nanocomposites.

To investigate the effects of the AC incorporation on the electrochemical characteristics of MoO_3/AC, we examined and compared the CV characteristics of MoO_3 and MoO_3/AC. Figures 5(a) and 5(b) present the CV curves of MoO_3 and MoO_3/AC, respectively. Both samples exhibited the typical oxidation and reduction peaks, representing the insertion and the desertion of electrolyte ions through the cathodic and the anodic reactions, respectively. The feature of the observed redox reaction belongs to the pseudocapacitive behavior, which would strongly affect the OER and HER activities. As the scan rate increased, the current density also increased because of the low diffusion resistance of the active catalyst material. Compared to bare MoO_3, MoO_3/AC displayed a larger CV window and a higher current density. This depicts that MoO_3/AC possesses a larger number of active sites than that of MoO_3. We believe such an improved electrochemical activity of MoO_3/AC to arise from two possible reasons. One is the increased electrical conductivity [17, 53], and the other is the increased active surface area [24, 102, 103]. The former will be discussed in detail later at the EIS part, and the latter is to be verified as follows.

To clarify the improved electrocatalytic performance of MoO_3/AC, firstly, we calculated the electrochemically active surface area (ECSA) by using the following equations [17, 24, 104, 105]:

$$J_{DL} = C_{DL} \times \frac{\nu}{A}, \tag{5}$$

$$\text{ECSA} = \frac{C_{DL}}{C_e}, \tag{6}$$

where J_{DL} is the double-layer charging current, C_{DL} is the non-Faradic capacitance, ν is the scan rate, A is the electrode area, and C_e is the electrolyte capacitance (0.04 mF/cm^2 for KOH). From the non-Faradic CV region, the magnitudes of ECSA were determined to be 124 and 153 cm^2 for MoO_3 and MoO_3/AC, respectively (Figures 5(c) and 5(d)). This

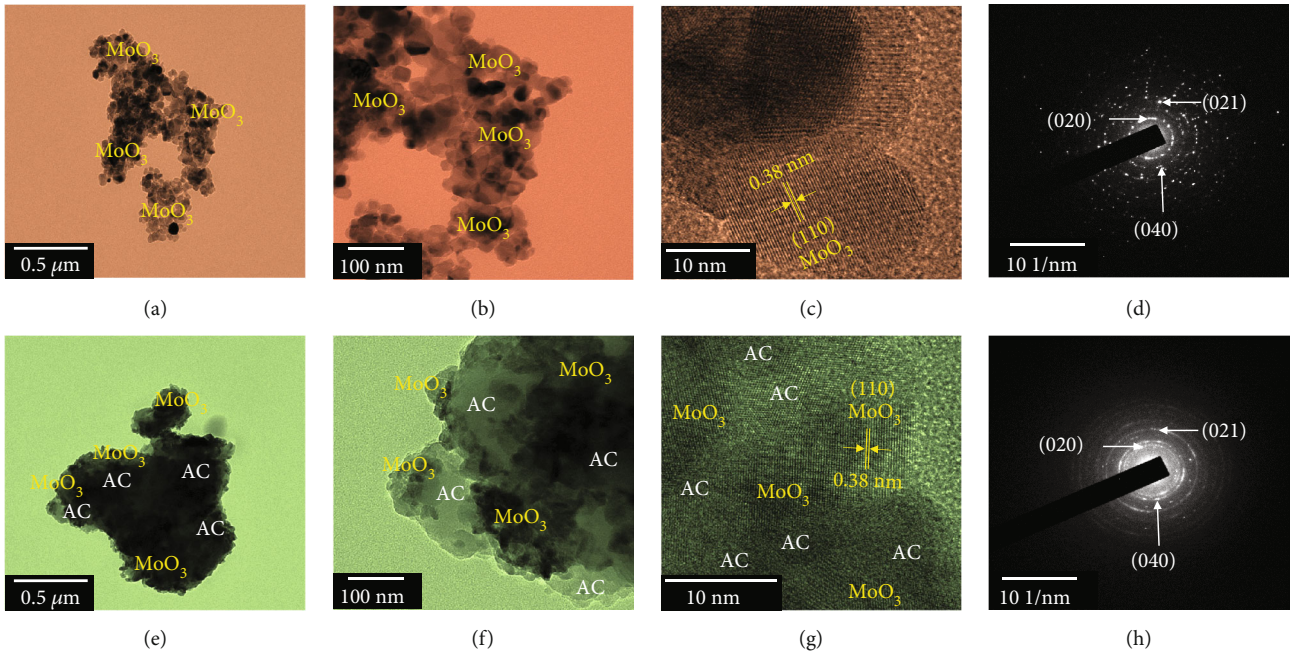

FIGURE 4: (a) Low- and (b) high-magnification bright-field TEM images, (c) high-resolution TEM image, and (d) SAED patterns of the MoO_3 nanoparticles. (e) Low- and (f) high-magnification bright-field TEM images, (g) high-resolution TEM image, and (h) SAED patterns of the MoO_3/AC nanocomposites.

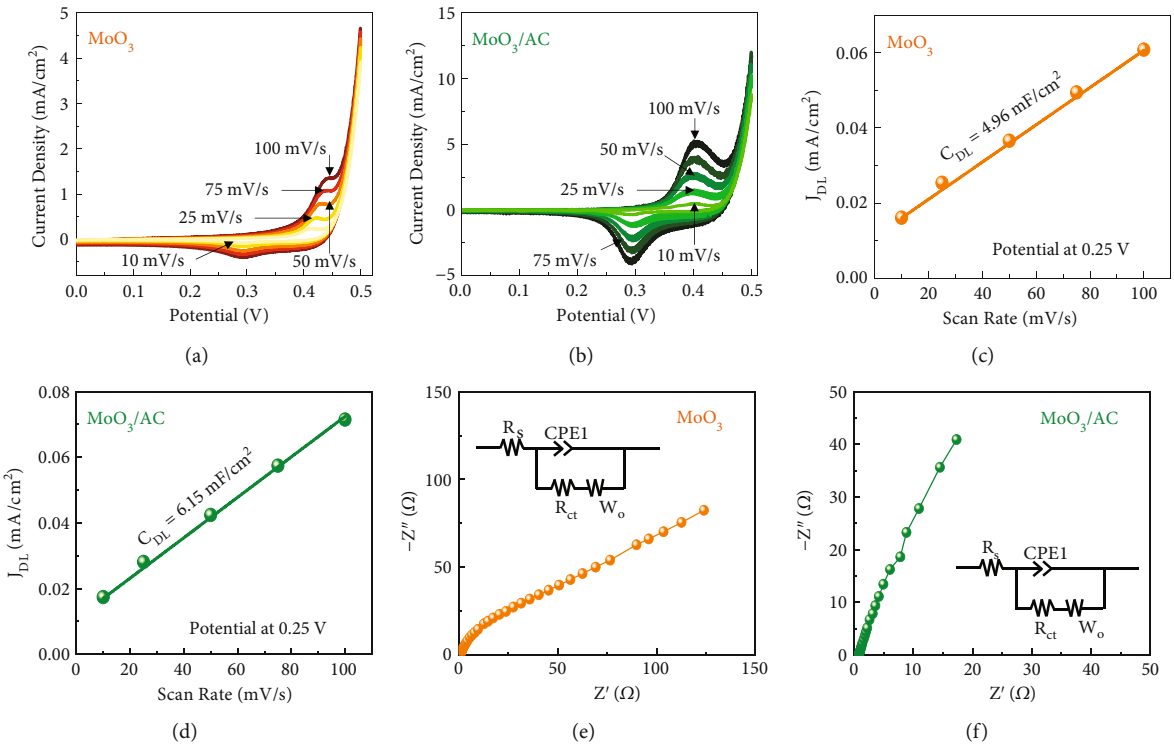

FIGURE 5: CV curves of the (a) MoO_3 and the (c) MoO_3/AC catalysts. J_{DL} as a function of the scan rate at 0.25 V for (c) MoO_3 and the (d) MoO_3/AC catalysts. Nyquist plots of the (e) MoO_3 and (f) MoO_3/AC catalysts and their corresponding equivalent circuits (insets of (e) and (f)).

depicts that MoO_3/AC has a larger number of the electrochemically active sites than that of MoO_3. One can ascribe such a result to the sonochemical exfoliation of the MoO_3 crystallites, as confirmed from FE-SEM, XRD, and TEM. In other words, since the smaller crystallites provide the larger surface-to-volume ratio, it can be inferred that the electrochemically active surface area was increased in MoO_3/AC *via* the sonochemical exfoliation of the MoO_3 crystallites.

Next, the electrochemical resistive behaviors were examined by the EIS measurements. As shown in the Nyquist

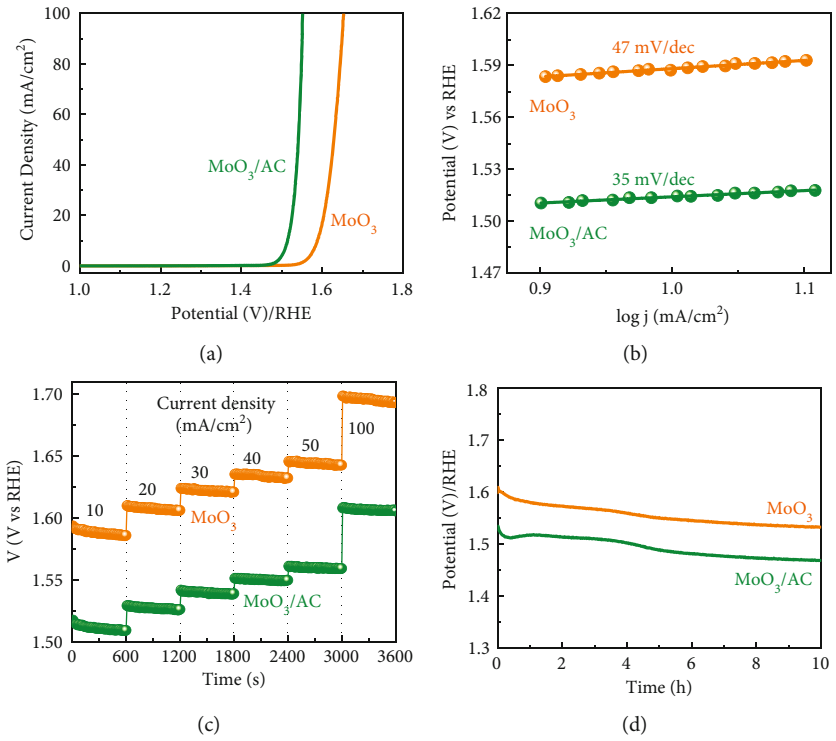

FIGURE 6: OER performances: (a) i_R-corrected LSV curves, (b) Tafel plots, (c) voltage-step profiles at different current densities (10 to 100 mA/cm^2), and (d) stability of the MoO_3 and the MoO_3/AC catalysts.

plots (Figures 5(e) and 5(f)), both MoO_3 and MoO_3/AC exhibited the straight lines and the parabolic curves at the low and the high frequency regions, respectively. The former is relevant to the series resistance (R_s) of the working electrodes, relating to the charge transfer resistance of the catalyst materials [18, 106]. The latter is attributed to the dispersion of electrolytes inside the working electrodes [24, 51]. Using the equivalent circuit model (insets of Figures 5(e) and 5(f)), the magnitudes of R_s were determined to be 4.02 and 1.06 Ω for MoO_3 and MoO_3/AC, respectively. Thus, one can surmise that MoO_3/AC has a smaller charge transfer resistance than that of bare MoO_3.

The increases in both the electrical conductivity and the active surface area help promote the fast electronic charge transport and the swift ionic diffusion, and it may in turn lead to the enhanced OER/HER activities. To assess the electrocatalytic OER/HER performances, therefore, we measured and compared the LSV characteristics for MoO_3 and MoO_3/AC. Figure 6(a) shows the i_R-corrected LSV curves at 1 mV/s of MoO_3 and MoO_3/AC. From the measured LSV data at 10 mA/cm^2, the overpotential (η) values of MoO_3 and MoO_3/AC were determined to be 350 and 280 mV, respectively, by using the following equations:

$$E_{RHE} = E_{SCE} + 0.059\,pH + E^0{}_{SCE}, \quad (7)$$

$$\eta = E_{RHE} - 1.23\,V\,(\text{for OER}), \quad (8)$$

$$\eta = E_{RHE}\,(\text{for HER}), \quad (9)$$

where E_{RHE} and E^0_{SCE} are the standard potentials of the reversible hydrogen electrode and the reference electrode, respectively. The η values obtained from the present MoO_3 and MoO_3/AC catalysts are comparable to and even lower than the literature values (Table S1). Particularly, MoO_3/AC recorded the lowest η among the well-known metal oxide-based electrocatalysts. For better understanding, we note that the turnover frequencies of MoO_3 and MoO_3/AC were estimated to be 0.019 and 0.712 s^{-1} at the potential of 1.51 V, respectively (Figure S4(a)). This implies the MoO_3/AC nanocomposites to hold the improved intrinsic reaction kinetics, which could enhance the OER performance in the alkaline electrolyte [17, 24, 38, 43]. The improved OER reaction kinetics can be further authenticated through evaluating the Tafel slope (S_T), which can be calculated by using the following equation:

$$\eta = S_T \log(J) + a, \quad (10)$$

where J and a are the current density applied to the electrodes and the fitting parameter, respectively. From the measured Tafel curves (Figure 6(b)), the small S_T values were determined for both MoO_3 (47 mV/dec) and MoO_3/AC (35 mV/dec). Particularly, MoO_3/AC exhibited to have a smaller S_T value, compared to other metal oxide-based electrocatalysts (Table S1). Namely, as discussed above, MoO_3/AC showed the improved intrinsic reaction kinetics because of its larger ECSA and smaller R_s.

The intrinsic reaction kinetics may also affect the chronopotentiometric responses. As shown in voltage-step profiles

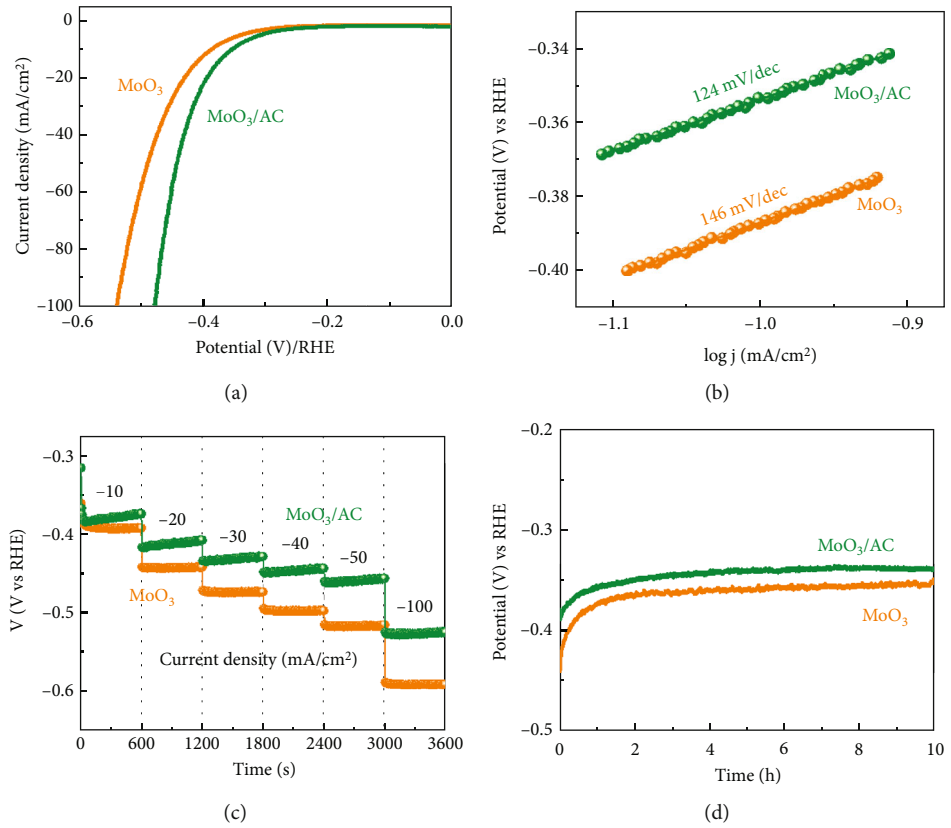

FIGURE 7: HER performances: (a) i_R-corrected LSV curves, (b) Tafel plots, (c) voltage-step profiles at different current densities (-10 to -100 mA/cm^2), and (d) stability of the MoO_3 and the MoO_3/AC catalysts.

(Figure 6(c)), MoO_3/AC showed the smaller overpotential values at every current density step than those of bare MoO_3. This validates that sonochemical hybridization of MoO_3/AC could help enhance the ion storage performance as well as the catalytic activity. In addition, MoO_3/AC showed the long-term stability, compared to MoO_3 (Figure 6(d)). Initially, both MoO_3 and MoO_3/AC revealed an enhanced potential activity because of the preliminary activation of the catalyst. After a few hours, however, the potential dramatically reduced and maintained constantly because of the catalyst stabilization. Furthermore, the sample showed the nearly identical LSV characteristics even after 10 h of the stability test (Figure S2). These suggest that MoO_3/AC could act as a superior and stable electrocatalytic OER catalyst.

Finally, we examined the HER performances to assess the bifunctional water electrolysis activities. Figure 7(a) displays the i_R-corrected LSV characteristic curves, which were measured in the KOH electrolyte at 1 mV/s. From LSV data at -10 mA/cm^2, the η values were calculated to be 387 and 353 mV for MoO_3 and MoO_3/AC, respectively. In addition, the low S_T values of 146 and 124 mV/dec were obtained from MoO_3 and MoO_3/AC, respectively, as can be seen from the Tafel curves (Figure 7(b)). Compared to bare MoO_3, the values of η and S_T of MoO_3/AC are comparable to and even smaller than those of other metal oxide-based electrocatalysts (Table S2). Furthermore, the turnover frequencies of the prepared MoO_3 and MoO_3/AC catalysts were calculated to be 0.00111 and 0.00184 s^{-1} at the potential of 0.35 V, respectively (Figure S4(b)). For the chronopotentiometric HER performance test (Figure 7(c)) and the stability test (Figure 7(d) and Figure S3), MoO_3/AC showed the better electrocatalytic activities than those of MoO_3. From all the above result, therefore, it can be concluded that sonochemical hybridization of orthorhombic α-MoO_3 and highly graphitized AC is of good use for improving the bifunctional OER/HER activities. For further improvements of both bifunctionality and stability, using the highly conductive and highly porous substrates (*e.g.*, Ni foam, C clothes, and C sheets) can also be the next step toward the practical OER/HER application of the MoO_3/AC catalyst.

4. Conclusions

The high-performance bifunctional OER/HER electrocatalysts of MoO_3/AC were fabricated through the facile ultrasonication by using the biomass-derived AC nanosheets and the sol-gel grown α-MoO_3 nanoparticles. MoO_3/AC exhibited the excellent electrocatalytic water splitting activities in both OER and HER. Namely, MoO_3/AC not only showed the superb OER performances (*i.e.*, low η of 280 mV and low S_T of 35 mV/dec) but also displayed the remarkable HER performances (*i.e.*, low η of 353 mV and low S_T of 124 mV/dec). Such excellent bifunctional OER/HER activities were confirmed to arise from the large ECSA (153 cm^2) and the R_s (1.06 Ω) of MoO_3/AC, attributing to sonochemical

hybridization of the highly conductive nanoconstituent (*i.e.*, graphitized AC nanosheets) and the electrochemically active nanoconstituent (*i.e.*, α-MoO_3 nanoparticles).

Data Availability

Data will be made available upon request.

Conflicts of Interest

The authors declare that they have no known competing financial interests or personal relationships that could have appeared to influence the work reported in this paper.

Authors' Contributions

Sankar Sekar carried out the investigation, formal analysis, methodology, and writing of the original draft. Ji-Seop Yun assisted in the investigation and formal analysis. Seoyeon Park carried out the investigation and formal analysis. Deuk Young Kim was responsible for the supervision and validation. Youngmin Lee made great contribution to data curation, methodology, and validation. Sejoon Lee assisted in the conceptualization, supervision, and funding acquisition and wrote, reviewed, and edited the manuscript.

Acknowledgments

This research was supported by the National Research Foundation (NRF) of Korea through the basic science research programs (2016R1A6A1A03012877 and 2023R1A2C1005421) funded by the Korean Government.

Supplementary Materials

Supplementary data includes the morphological and the structural properties of the AC nanosheets, the electrocatalytic properties of MoO_3 and MoO_3/AC, and the comparison of the electrocatalytic OER and HER activities for various materials. Figure S1: FE-SEM image of the AC nanosheets. Figure S2: LSV curves of MoO_3 and MoO_3/AC for OER before and after the stability test. Figure S3: LSV curves of MoO_3 and MoO_3/AC for HER before and after the stability test. Figure S4: turnover frequency plots of MoO_3 and MoO_3/AC for OER and HER. Table S1: comparison of the OER performances of MoO_3 and MoO_3/AC with previously reported metal oxide-based electrocatalysts. Table S2: comparison of the HER performances of MoO_3 and MoO_3/AC with previously reported metal oxide-based electrocatalysts. *(Supplementary Materials)*

References

[1] S. Chu and A. Majumdar, "Opportunities and challenges for a sustainable energy future," *Nature*, vol. 488, no. 7411, pp. 294–303, 2012.

[2] J. Guo, Y. Zhang, A. Zavabeti et al., "Hydrogen production from the air," *Nature Communications*, vol. 13, no. 1, p. 5046, 2022.

[3] Y. Liu, R. Zou, B. Qin, J. Gan, and X. Peng, "Energy-efficient monosaccharides electrooxidation coupled with green hydrogen production by bifunctional Co_9S_8/Ni_3S_2 electrode," *Chemical Engineering Journal*, vol. 446, article 136950, 2022.

[4] Z. Chen, W. Wei, L. Song, and B. J. Ni, "Hybrid water electrolysis: a new sustainable avenue for energy-saving hydrogen production," *Sustainable Horizons*, vol. 1, article 100002, 2022.

[5] S. Wang, A. Lu, and C. J. Zhong, "Hydrogen production from water electrolysis: role of catalysts," *Nano Convergence*, vol. 8, no. 1, p. 4, 2021.

[6] B. You and Y. Sun, "Innovative strategies for electrocatalytic water splitting," *Accounts of Chemical Research*, vol. 51, no. 7, pp. 1571–1580, 2018.

[7] A. Raveendran, M. Chandran, and R. Dhanusuraman, "A comprehensive review on the electrochemical parameters and recent material development of electrochemical water splitting electrocatalysts," *RSC Advances*, vol. 13, no. 6, pp. 3843–3876, 2023.

[8] M. El Ouardi, A. El Idrissi, H. A. Ahsaine, A. BaQais, M. Saadi, and M. Arab, "Current advances on nanostructured oxide photoelectrocatalysts for water splitting: a comprehensive review," *Surfaces and Interfaces*, vol. 45, article 103850, 2024.

[9] E. Antolini, "Iridium as catalyst and cocatalyst for oxygen evolution/reduction in acidic polymer electrolyte membrane electrolyzers and fuel cells," *ACS Catalysis*, vol. 4, no. 5, pp. 1426–1440, 2014.

[10] X. Li, L. Zhao, J. Yu et al., "Water splitting: from electrode to green energy system," *Nano-Micro Letters*, vol. 12, no. 1, p. 131, 2020.

[11] A. Barhoum, H. H. El-Maghrabi, A. A. Nada et al., "Simultaneous hydrogen and oxygen evolution reactions using free-standing nitrogen-doped-carbon–Co/CoOx nanofiber electrodes decorated with palladium nanoparticles," *Journal of Materials Chemistry A*, vol. 9, no. 33, pp. 17724–17739, 2021.

[12] R. Manikandan, S. Sadhasivam, S. Lee et al., "Deep eutectic solvents assisted synthesis of AC-decorated NiO nanocomposites for hydrogen evolution reaction," *Journal of Molecular Liquids*, vol. 375, article 121338, 2023.

[13] S. Sekar, S. Brindha Devi, S. Maruthasalamoorthy et al., "One-step facile hydrothermal synthesis of rGO-CoS_2 nanocomposites for high performance HER electrocatalysts," *International Journal of Hydrogen Energy*, vol. 47, no. 95, pp. 40359–40367, 2022.

[14] R. Manikandan, S. Sekar, S. P. Mani, S. Lee, D. Y. Kim, and S. Saravanan, "Bismuth tungstate-anchored PEDOT: PSS materials for high performance HER electrocatalyst," *International Journal of Hydrogen Energy*, vol. 48, no. 31, pp. 11746–11753, 2023.

[15] A. Tahir, F. Arshad, T. . Haq, I. Hussain, S. Z. Hussain, and H. . Rehman, "Roles of metal oxide nanostructure-based substrates in sustainable electrochemical water splitting: recent development and future perspective," *ACS Applied Nano Materials*, vol. 6, no. 3, pp. 1631–1647, 2023.

[16] M. Plevová, J. Hnát, and K. Bouzek, "Electrocatalysts for the oxygen evolution reaction in alkaline and neutral media. A comparative review," *Journal of Power Sources*, vol. 507, article 230072, 2021.

[17] S. Sekar, A. T. Aqueel Ahmed, S. M. Pawar et al., "Enhanced water splitting performance of biomass activated carbon-

anchored WO_3 nanoflakes," *Applied Surface Science*, vol. 508, article 145127, 2020.

[18] S. Sekar, D. H. Sim, and S. Lee, "Excellent electrocatalytic hydrogen evolution reaction performances of partially graphitized activated-carbon nanobundles derived from biomass human hair wastes," *Nanomaterials*, vol. 12, no. 3, p. 531, 2022.

[19] M. El Ouardi, A. El Idrissi, M. Arab et al., "Review of photoelectrochemical water splitting: from quantitative approaches to effect of sacrificial agents, oxygen vacancies, thermal and magnetic field on (photo)electrolysis," *International Journal of Hydrogen Energy*, vol. 51, pp. 1044–1067, 2024.

[20] J. Li, "Oxygen evolution reaction in energy conversion and storage: design strategies under and beyond the energy scaling relationship," *Nano-Micro Letters*, vol. 14, no. 1, p. 112, 2022.

[21] A. Barhoum, H. H. El-Maghrabi, I. Iatsunskyi et al., "Atomic layer deposition of Pd nanoparticles on self-supported carbon-Ni/NiO-Pd nanofiber electrodes for electrochemical hydrogen and oxygen evolution reactions," *Journal of Colloid and Interface Science*, vol. 569, pp. 286–297, 2020.

[22] H. H. El-Maghrabi, A. A. Nada, M. F. Bekheet et al., "Coaxial nanofibers of nickel/gadolinium oxide/nickel oxide as highly effective electrocatalysts for hydrogen evolution reaction," *Journal of Colloid and Interface Science*, vol. 587, pp. 457–466, 2021.

[23] S. Kawrani, M. Boulos, M. F. Bekheet et al., "Segregation of copper oxide on calcium copper titanate surface induced by graphene oxide for water splitting applications," *Applied Surface Science*, vol. 516, article 146051, 2020.

[24] S. Sekar, D. Kim, and S. Lee, "Excellent oxygen evolution reaction of activated carbon-anchored NiO nanotablets prepared by green routes," *Nanomaterials*, vol. 10, no. 7, p. 1382, 2020.

[25] P. Liu, C. Sun, G. Liu, Z. Jiang, and H. Zhao, "Ultra-small-sized multi-element metal oxide nanofibers: an efficient electrocatalyst for hydrogen evolution," *Nanoscale Advances*, vol. 4, no. 7, pp. 1758–1769, 2022.

[26] H. H. El-Maghrabi, A. A. Nada, S. Roualdes, and M. F. Bekheet, "Design of Ni/NiO-TiO_2/rGO nanocomposites on carbon cloth conductors via PECVD for electrocatalytic water splitting," *International Journal of Hydrogen Energy*, vol. 45, no. 56, pp. 32000–32011, 2020.

[27] S. Kawrani, A. A. Nada, M. F. Bekheet et al., "Enhancement of calcium copper titanium oxide photoelectrochemical performance using boron nitride nanosheets," *Journal of Chemical Engineering*, vol. 389, article 124326, 2020.

[28] S. Sekar, S. Park, J. Jung, and S. Lee, "Superb bifunctional water electrolysis activities of carbon nanotube-decorated lanthanum hydroxide nanocomposites," *International Journal of Energy Research*, vol. 2023, Article ID 6685726, 13 pages, 2023.

[29] M. Tariq, W. Q. Zaman, W. Sun et al., "Unraveling the beneficial electrochemistry of IrO_2/MoO_3 hybrid as a highly stable and efficient oxygen evolution reaction catalyst," *ACS Sustainable Chemistry & Engineering*, vol. 6, no. 4, pp. 4854–4862, 2018.

[30] P. F. Liu, S. Yang, L. R. Zheng, B. Zhang, and H. G. Yang, "Mo^{6+} activated multimetal oxygen-evolving catalysts," *Chemical Science*, vol. 8, no. 5, pp. 3484–3488, 2017.

[31] Y. Zhu, Y. Yao, Z. Luo et al., "Nanostructured MoO_3 for efficient energy and environmental catalysis," *Molecules*, vol. 25, no. 1, p. 18, 2020.

[32] M. Tariq, Y. Wu, C. Ma et al., "Boosted up stability and activity of oxygen vacancy enriched RuO_2/MoO_3 mixed oxide composite for oxygen evolution reaction," *International Journal of Hydrogen Energy*, vol. 45, no. 35, pp. 17287–17298, 2020.

[33] A. V. Avani and E. I. Anila, "Recent advances of MoO_3 based materials in energy catalysis: applications in hydrogen evolution and oxygen evolution reactions," *International Journal of Hydrogen Energy*, vol. 47, no. 47, pp. 20475–20493, 2022.

[34] Ø. S. Fjellvåg, A. Ruud, H. H. Sønsteby, O. Nilsen, and H. Fjellvåg, "Crystallization, phase stability, and electrochemical performance of β-MoO_3 thin films," *Crystal Growth & Design*, vol. 20, no. 6, pp. 3861–3866, 2020.

[35] C. D. A. Lima, J. V. B. Moura, G. S. Pinheiro et al., "Co-doped α-MoO_3 hierarchical microrods: synthesis, structure and phonon properties," *Ceramics International*, vol. 47, no. 19, pp. 27778–27788, 2021.

[36] Y. Niu, H. Su, X. Li, J. Li, and Y. Qi, "Synthesis of porous α-MoO_3 microspheres as electrode materials for supercapacitors," *Journal of Alloys and Compounds*, vol. 898, p. 162863, 2022.

[37] R. S. Datta, F. Haque, M. Mohiuddin et al., "Highly active two dimensional α-MoO_{3-x} for the electrocatalytic hydrogen evolution reaction," *Journal of Materials Chemistry A*, vol. 5, no. 46, pp. 24223–24231, 2017.

[38] M. Zhang, R. Li, D. Hu, X. Huang, Y. Liu, and K. Yan, "Porous molybdenum trioxide as a bifunctional electrocatalyst for oxygen and hydrogen evolution," *Journal of Electroanalytical Chemistry*, vol. 836, pp. 102–106, 2019.

[39] M. Santos-Beltrán, C. Ornelas, J. Lara-Romero, and F. Paraguay-Delgado, "Molybdenum oxide particles for dye removal and tribology," *Materials Letters*, vol. 291, p. 129544, 2021.

[40] H. Hu, C. Deng, J. Xu, K. Zhang, and M. Sun, "Metastable h-MoO_3 and stable α-MoO_3 microstructures: controllable synthesis, growth mechanism and their enhanced photocatalytic activity," *Journal of Experimental Nanoscience*, vol. 10, no. 17, pp. 1336–1346, 2015.

[41] A. S. Etman, H. N. Abdelhamid, Y. Yuan, L. Wang, X. Zou, and J. Sun, "Facile water-based strategy for synthesizing MoO_{3-x} nanosheets: efficient visible light photocatalysts for dye degradation," *ACS Omega*, vol. 3, no. 2, pp. 2193–2201, 2018.

[42] Q.-Y. Ouyang, L. Li, Q.-S. Wang et al., "Facile synthesis and enhanced H_2S sensing performances of Fe-doped α-MoO_3 micro-structures," *Sensors and Actuators B: Chemical*, vol. 169, pp. 17–25, 2012.

[43] S. D. Raut, N. M. Shinde, B. G. Ghule et al., "Room-temperature solution-processed sharp-edged nanoshapes of molybdenum oxide for supercapacitor and electrocatalysis applications," *Chemical Engineering Journal*, vol. 433, article 133627, 2022.

[44] A. A. Bortoti, A. F. Gavanski, Y. R. Velazquez, A. Galli, and E. G. de Castro, "Facile and low cost oxidative conversion of MoS_2 in α-MoO_3: synthesis, characterization and application," *Journal of Solid State Chemistry*, vol. 252, pp. 111–118, 2017.

[45] A. L. Al-Otaibi, "Yttrium doped single-crystalline orthorhombic molybdenum oxide micro-belts: synthesis, structural, optical and photocatalytic properties," *Journal of Inorganic and Organometallic Polymers and Materials*, vol. 31, no. 8, pp. 3416–3429, 2021.

[46] A. P. Amrute, A. Bordoloi, N. Lucas, K. Palraj, and S. B. Halligudi, "Sol–Gel Synthesis of MoO_3/SiO_2 composite for catalytic application in condensation of anisole with paraformaldehyde," *Catalysis Letters*, vol. 126, no. 3-4, pp. 286–292, 2008.

[47] I. Shaheen and K. S. Ahmad, "Modified sol gel synthesis of MoO_3 NPs using organic template: synthesis, characterization and electrochemical investigations," *Journal of Sol-Gel Science and Technology*, vol. 97, no. 1, pp. 178–190, 2021.

[48] N. Naresh, P. Jena, and N. Satyanarayana, "Facile synthesis of MoO_3/rGO nanocomposite as anode materials for high performance lithium-ion battery applications," *Journal of Alloys and Compounds*, vol. 810, article 151920, 2019.

[49] X. Wang, Y. Xie, K. Tang, C. Wang, and C. Yan, "Redox chemistry of molybdenum trioxide for ultrafast hydrogen-ion storage," *Angewandte Chemie, International Edition*, vol. 57, no. 36, pp. 11569–11573, 2018.

[50] H. Sun, D. Hanlon, D. A. Dinh et al., "Carbon nanotubes-bridged molybdenum trioxide nanosheets as high performance anode for lithium ion batteries," *2D Materials*, vol. 5, no. 1, article 015024, 2018.

[51] C. Huang, C. Pi, X. Zhang et al., "In situ synthesis of MoP nanoflakes intercalated N-doped graphene nanobelts from MoO_3–amine hybrid for high-efficient hydrogen evolution reaction," *Small*, vol. 14, no. 25, article 1800667, 2018.

[52] S. Bashir, A. Habib, A. Jamil, A. Alazmi, and M. Shahid, "Fabrication of Ag-doped MoO_3 and its nanohybrid with a two-dimensional carbonaceous material to enhance photocatalytic activity," *Advanced Powder Technology*, vol. 33, no. 3, article 103482, 2022.

[53] D. N. Sangeetha, R. S. Holla, B. Ramachandra Bhat, and M. Selvakumar, "High power density and improved H_2 evolution reaction on MoO_3/activated carbon composite," *International Journal of Hydrogen Energy*, vol. 45, no. 13, pp. 7801–7812, 2020.

[54] H. Demiral, İ. Demiral, B. Karabacakoğlu, and F. Tümsek, "Production of activated carbon from olive bagasse by physical activation," *Chemical Engineering Research and Design*, vol. 89, no. 2, pp. 206–213, 2011.

[55] A. L. Ahmad, M. M. Loh, and J. A. Aziz, "Preparation and characterization of activated carbon from oil palm wood and its evaluation on methylene blue adsorption," *Dyes and Pigments*, vol. 75, no. 2, pp. 263–272, 2007.

[56] S. Sankar, A. T. A. Ahmed, A. I. Inamdar et al., "Biomass-derived ultrathin mesoporous graphitic carbon nanoflakes as stable electrode material for high-performance supercapacitors," *Materials and Design*, vol. 169, p. 107688, 2019.

[57] B. K. Hamad, A. M. Noor, A. R. Afida, and M. N. Mohd Asri, "High removal of 4-chloroguaiacol by high surface area of oil palm shell-activated carbon activated with NaOH from aqueous solution," *Desalination*, vol. 257, no. 1-3, pp. 1–7, 2010.

[58] S. Sankar, H. Lee, H. Jung et al., "Ultrathin graphene nanosheets derived from rice husks for sustainable supercapacitor electrodes," *New Journal of Chemistry*, vol. 41, no. 22, pp. 13792–13797, 2017.

[59] M. Gale, T. Nguyen, M. Moreno, and K. L. Gilliard-AbdulAziz, "Physiochemical properties of biochar and activated carbon from biomass residue: influence of process conditions to adsorbent properties," *ACS Omega*, vol. 6, no. 15, pp. 10224–10233, 2021.

[60] S. Sekar, C. Bathula, I. Rabani et al., "Enhanced photocatalytic crystal-violet degradation performances of sonochemically-synthesized AC-CeO_2 nanocomposites," *Ultrasonics Sonochemistry*, vol. 90, p. 106177, 2022.

[61] S. Sekar, V. Preethi, V. S. Srivishnu, S. Saravanan, and S. Lee, "Highly-efficient photocatalytic activity of TiO_2-AC nanocomposites for hydrogen production from sulphide wastewater," *International Journal of Hydrogen Energy*, vol. 47, no. 95, pp. 40275–40285, 2022.

[62] S. K. Arumugasamy, G. Chellasamy, S. Sekar, S. Lee, S. Govindaraju, and K. Yun, "TriMOF synergized on the surface of activated carbon produced from pineapple leaves for the environmental pollutant reduction and oxygen evolution process," *Chemosphere*, vol. 286, article 131893, Part 3, 2022.

[63] S. Sekar, I. Rabani, C. Bathula et al., "Graphitic carbon-encapsulated V_2O_5 nanocomposites as a superb photocatalyst for crystal violet degradation," *Environmental Research*, vol. 205, p. 112201, 2022.

[64] V. C. Hoang, K. N. Dinh, and V. G. Gomes, "Hybrid Ni/NiO composite with N-doped activated carbon from waste cauliflower leaves: a sustainable bifunctional electrocatalyst for efficient water splitting," *Carbon*, vol. 157, pp. 515–524, 2020.

[65] X. Kou, X. Xin, Y. Zhang, and L.-Y. Meng, "Facile synthesis of nitrogen-doped carbon dots (N-CDs) and N-CDs/NiO composite as an efficient electrocatalyst for oxygen evolution reaction," *Carbon Letters*, vol. 31, no. 4, pp. 695–706, 2021.

[66] W. Yaseen, M. Xie, B. A. Yusuf et al., "Hierarchical Co/MoO_2@N-doped carbon nanosheets derived from waste lotus leaves for electrocatalytic water splitting," *International Journal of Hydrogen Energy*, vol. 47, no. 35, pp. 15673–15686, 2022.

[67] J. Zhu, S. Tang, H. Xie, Y. Dai, and X. Meng, "Hierarchically porous MnO_2 microspheres doped with homogeneously distributed Fe_3O_4 nanoparticles for supercapacitors," *ACS Applied Materials & Interfaces*, vol. 6, no. 20, pp. 17637–17646, 2014.

[68] Y. Dai, S. Tang, S. Vongehr, and X. Meng, "Silver nanoparticle-induced growth of nanowire-covered porous MnO_2 spheres with superior supercapacitance," *ACS Sustainable Chemistry & Engineering*, vol. 2, no. 4, pp. 692–698, 2014.

[69] S. Sankar, A. I. Inamdar, H. Im, S. Lee, and D. Y. Kim, "Template-free rapid sonochemical synthesis of spherical α-MnO_2 nanoparticles for high-energy supercapacitor electrode," *Ceramics International*, vol. 44, no. 14, pp. 17514–17521, 2018.

[70] N. G. Prakash, M. Dhananjaya, A. L. Narayana, H. Maseed, V. V. S. S. Srikanth, and O. M. Hussain, "Improved electrochemical performance of rGO-wrapped MoO_3 nanocomposite for supercapacitors," *Applied Physics A*, vol. 125, no. 8, p. 488, 2019.

[71] Y. Liu, P. Feng, Z. Wang, X. Jiao, and F. Akhtar, "Novel fabrication and enhanced photocatalytic MB degradation of hierarchical porous monoliths of MoO_3 nanoplates," *Scientific Reports*, vol. 7, no. 1, p. 1845, 2017.

[72] S. Bai, C. Chen, R. Luo, A. Chen, and D. Li, "Synthesis of MoO_3/reduced graphene oxide hybrids and mechanism of enhancing H_2S sensing performances," *Sensors and Actuators B: Chemical*, vol. 216, pp. 113–120, 2015.

[73] M. B. Rahmani, S. H. Keshmiri, J. Yu et al., "Gas sensing properties of thermally evaporated lamellar MoO_3," *Sensors and Actuators B: Chemical*, vol. 145, no. 1, pp. 13–19, 2010.

[74] S. Sekar, S. Kumar, Y. Lee et al., "Excellent nitroarene reduction activity of ilmenite nanochips prepared by facile template-free hydrothermal synthesis," *Ceramics International*, vol. 48, no. 19, pp. 29421–29428, 2022.

[75] S. Lee, T. Won Kang, and D. Y. Kim, "Correlation of magnetic properties with microstructural properties for columnar-structured $(Zn_{1-x}Mn_x)O/Al_2O_3$ (0 0 0 1) thin films," *Journal of Crystal Growth*, vol. 284, no. 1–2, pp. 6–14, 2005.

[76] V. Jadkar, A. Pawbake, R. Waykar et al., "Synthesis of orthorhombic-molybdenum trioxide (α-MoO_3) thin films by hot wire-CVD and investigations of its humidity sensing properties," *Journal of Materials Science: Materials in Electronics*, vol. 28, no. 21, pp. 15790–15796, 2017.

[77] X. Tan, L. Wang, C. Cheng, X. Yan, B. Shen, and J. Zhang, "Plasmonic MoO_{3-x}@MoO_3 nanosheets for highly sensitive SERS detection through nanoshell-isolated electromagnetic enhancement," *Chemical Communications*, vol. 52, no. 14, pp. 2893–2896, 2016.

[78] S. Swathi, G. Ravi, R. Yuvakkumar et al., "Water-splitting application of orthorhombic molybdite α-MoO_3 nanorods," *Ceramics International*, vol. 46, no. 14, pp. 23218–23222, 2020.

[79] J. Z. Ou, J. L. Campbell, D. Yao, W. Wlodarski, and K. Kalantar-zadeh, "*In situ* Raman spectroscopy of H_2 gas interaction with layered MoO_3," *Journal of Physical Chemistry C*, vol. 115, no. 21, pp. 10757–10763, 2011.

[80] G. Mestl, P. Ruiz, B. Delmon, and H. Knozinger, "Oxygen-exchange properties of MoO_3: an in situ Raman spectroscopy study," *The Journal of Physical Chemistry*, vol. 98, no. 44, pp. 11269–11275, 1994.

[81] M. Dieterle, G. Weinberg, and G. Mestl, "Raman spectroscopy of molybdenum oxides," *Physical Chemistry Chemical Physics*, vol. 4, no. 5, pp. 812–821, 2002.

[82] S. Sekar, S. Lee, P. Vijayarengan et al., "Upcycling of wastewater via effective photocatalytic hydrogen production using MnO_2 nanoparticles—decorated activated carbon nanoflakes," *Nanomaterials*, vol. 10, no. 8, p. 1610, 2020.

[83] S. Sekar, Y. Lee, D. Y. Kim, and S. Lee, "Substantial LIB anode performance of graphitic carbon nanoflakes derived from biomass green-tea waste," *Nanomaterials*, vol. 9, no. 6, p. 871, 2019.

[84] S. Lee and Y. Lee, "Graphene/lead-zirconate-titanate ferroelectric memory devices with tenacious retention characteristics," *Carbon*, vol. 126, pp. 176–182, 2018.

[85] S. Lee, Y. Lee, D. Young Kim, E. B. Song, and S. Min Kim, "Back-gate tuning of Schottky barrier height in graphene/zinc-oxide photodiodes," *Applied Physics Letters*, vol. 102, no. 24, article 242114, 2013.

[86] S. Lee, Y. Lee, S. M. Kim, and E. B. Song, "Fully-transparent graphene charge-trap memory device with large memory window and long-term retention," *Carbon*, vol. 127, pp. 70–76, 2018.

[87] S. Lee, E. B. Song, S. Kim et al., "Impact of gate work-function on memory characteristics in $Al_2O_3/HfO_x/Al_2O_3$/graphene charge-trap memory devices," *Applied Physics Letters*, vol. 100, no. 2, article 023109, 2012.

[88] S. Lee, E. B. Song, S. Min Kim et al., "Reduced electron back-injection in $Al_2O_3/AlO_x/Al_2O_3$/graphene charge-trap memory devices," *Applied Physics Letters*, vol. 101, no. 24, article 243109, 2012.

[89] Y. Lee, D. Y. Kim, and S. Lee, "Low-power graphene/ZnO Schottky UV photodiodes with enhanced lateral schottky barrier homogeneity," *Nanomaterials*, vol. 9, no. 5, p. 799, 2019.

[90] O. O. Kapitanova, E. V. Emelin, S. G. Dorofeev et al., "Direct patterning of reduced graphene oxide/graphene oxide memristive heterostructures by electron-beam irradiation," *Journal of Materials Science & Technology*, vol. 38, pp. 237–243, 2020.

[91] L. M. Malard, M. A. Pimenta, G. Dresselhaus, and M. S. Dresselhaus, "Raman spectroscopy in graphene," *Physics Reports*, vol. 473, no. 5-6, pp. 51–87, 2009.

[92] Y. Bleu, F. Bourquard, A.-S. Loir, V. Barnier, F. Garrelie, and C. Donnet, "Raman study of the substrate influence on graphene synthesis using a solid carbon source via rapid thermal annealing," *Journal of Raman Specroscopy*, vol. 50, no. 11, pp. 1630–1641, 2019.

[93] Y. Mizukoshi, R. Oshima, Y. Maeda, and Y. Nagata, "Preparation of platinum nanoparticles by sonochemical reduction of the Pt(II) ion," *Langmuir*, vol. 15, no. 8, pp. 2733–2737, 1999.

[94] J. Zhang, J. Du, B. Han, Z. Liu, T. Jiang, and Z. Zhang, "Sonochemical formation of single-crystalline gold nanobelts," *Angewandte Chemie, International Edition*, vol. 45, no. 7, pp. 1116–1119, 2006.

[95] J. H. Bang and K. S. Suslick, "Applications of ultrasound to the synthesis of nanostructured materials," *Advanced Materials*, vol. 22, no. 10, pp. 1039–1059, 2010.

[96] A. Nemamcha, J.-L. Rehspringer, and D. Khatmi, "Synthesis of palladium nanoparticles by sonochemical reduction of palladium(II) nitrate in aqueous solution," *Journal of Physical Chemistry B*, vol. 110, no. 1, pp. 383–387, 2006.

[97] C.-H. Su, P.-L. Wu, and C.-S. Yeh, "Sonochemical synthesis of well-dispersed gold nanoparticles at the ice temperature," *Journal of Physical Chemistry B*, vol. 107, no. 51, pp. 14240–14243, 2003.

[98] T. He, Y. Wu, C. Jiang et al., "Novel magnetic Fe_3O_4/g-C_3N_4/MoO_3 nanocomposites with highly enhanced photocatalytic activities: visible-light-driven degradation of tetracycline from aqueous environment," *PLoS One*, vol. 15, no. 8, article e0237389, 2020.

[99] J. Li and X. Liu, "Preparation and characterization of α-MoO_3 nanobelt and its application in supercapacitor," *Materials Letters*, vol. 112, pp. 39–42, 2013.

[100] P. K. Bankar, L. N. Khandare, D. J. Late, and M. A. More, "Enhanced field emission performance of MoO_3 nanorods and MoO_3-rGO nanocomposite," *ChemistrySelect*, vol. 2, no. 33, pp. 10912–10917, 2017.

[101] S. Sankar, S. Saravanan, A. T. A. Ahmed et al., "Spherical activated-carbon nanoparticles derived from biomass green tea wastes for anode material of lithium-ion battery," *Materials Letters*, vol. 240, pp. 189–192, 2019.

[102] X. Du, W. Fu, P. Su, Q. Zhang, and M. Zhou, "FeMo@porous carbon derived from MIL-53(Fe)@MoO_3 as excellent heterogeneous electro-Fenton catalyst: co-catalysis of Mo," *Journal of Environmental Sciences*, vol. 127, pp. 652–666, 2023.

[103] Z. Hou, D. Yang, Y. Xin et al., "In situ coupled MoO_3 with CoP/rGO to construct three-dimensional self-supported catalyst for highly efficient alkaline hydrogen evolution reaction," *Journal of Materials Science and Technology*, vol. 104, pp. 194–201, 2022.

[104] C. C. L. McCrory, S. Jung, J. C. Peters, and T. F. Jaramillo, "Benchmarking heterogeneous electrocatalysts for the oxygen evolution reaction," *Journal of the American Chemical Society*, vol. 135, no. 45, pp. 16977–16987, 2013.

[105] S. Sekar, S. Sadhasivam, E. K. Nangai, S. Saravanan, D. Y. Kim, and S. Lee, "Enhanced hydrogen evolution reaction performances of ultrathin $CuBi_2O_4$ nanoflakes," *International Journal of Energy Research*, vol. 2023, Article ID 5038466, 10 pages, 2023.

[106] K. Li, J. Ma, X. Guan et al., "3D self-supported $Ni(PO_3)_2$–MoO_3 nanorods anchored on nickel foam for highly efficient overall water splitting," *Nanoscale*, vol. 10, no. 47, pp. 22173–22179, 2018.